# Controlling the Effective Surface Area and Pore Size Distribution of sp^2 Carbon Materials and Their Impact on the Capacitance Performance of These Materials

Long Zhang, Xi Yang, Fan Zhang, Guankui Long, Tengfei Zhang, Kai Leng, Yawei Zhang, Yi Huang, Yanfeng Ma, Mingtao Zhang, and Yongsheng Chen*

The Key Laboratory for Functional Polymer Materials and Centre for Nanoscale Science and Technology, Institute of Polymer Chemistry, College of Chemistry, Nankai University, Tianjin 300071, China

S *Supporting Information*
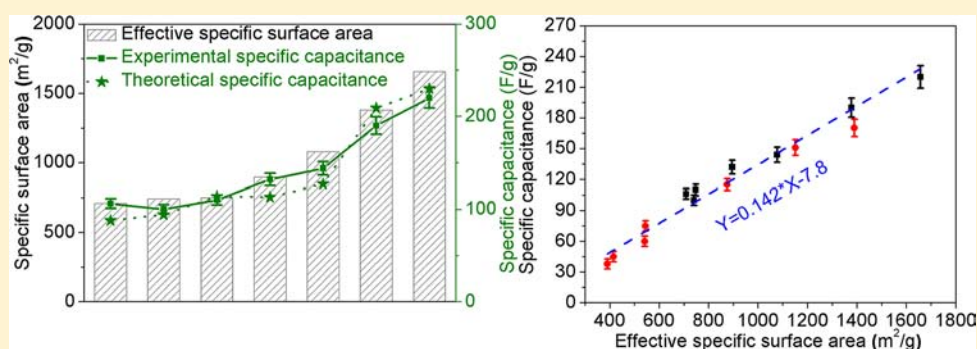
ABSTRACT: A series of sp^2 carbon materials with different specific surface area (SSA) and controlled pore size distribution (PSD) were synthesized at large scale through a facile and low-cost method. The SSA and PSD of these carbon materials were controlled by using different carbon sources and preparation methods. With different total and effective SSA (E-SSA) and PSD, the impacts on their capacitance performance were investigated thoroughly, which demonstrated that both E-SSA and PSD played the most important roles in their capacitance performance. Furthermore, theoretical modeling was performed, and the results are in agreement with the experimental results for the influence of E-SSA and PSD on their capacitance performance. Based on these, a general model using the slit/cylindrical NL-DFT approach is proposed for the estimation of the specific capacitance of sp^2 carbon materials, which offers a simple but reliable method to predict the capacitance performance of these materials, thus speeding up the design and screening of the materials for high-performance supercapacitor and other surface area related devices.

■ INTRODUCTION

Supercapacitors based on sp^2 carbon materials have attracted tremendous attention in both theoretical and practical application studies for their high power density, superior performance in extreme temperatures, and outstanding cycle stability.[1−6] During the past several years, most efforts have been focusing on increasing the specific capacitance and operating voltage of carbon-based supercapacitors to achieve higher energy density,[1,7] which can make carbon-based supercapacitors more capable for the primary power sources to replace batteries.[8−10] Since the operating voltage is simply determined/limited by the electrolytes[1,11] but the specific capacitance of carbon materials is more complicated and dependent on many factors such as specific surface area (SSA), pore size distribution (PSD) and conductivity of carbon materials, thus more efforts have been devoted on increasing specific capacitance of carbon materials, such as using carbon materials with high SSA ranging from ∼1000 to more than 3000 m^2/g.[2,8,9,12−17]

However, for those high surface area materials used for supercapacitor applications, such as that based on the activated carbon (AC) materials,[18−20] total SSA is unfortunately but generally used and discussed for their capacitance performance. This unavoidably often gives wrong impression since it is the effective specific surface area (E-SSA) which is accessible to the electrolyte ions and eventually determines the fundamental performance.[11,21] As we know, the E-SSA is determined by both the total SSA and the PSD of carbon materials based on the electrolyte ion sizes.[9] Therefore, thorough investigation is much needed to explore the controlling of both SSA and PSD of sp^2 carbon-based materials for more effective material design with better capacitance performance.

Indeed, some elegant works have been reported in this regard using the carbon materials prepared from template approach for studying the influence of SSA and PSD on the capacitance

performance.[15,22−24] The most important advantage of this approach is that the materials obtained have rather narrow distribution of SSA and pore size, which obviously facilitate the studies and simply the modeling. Nevertheless, a wide scope of materials, which have different and wide but controlled range of SSA (including the E-SSA) and PSD and are easily prepared in large quantity are much needed to have a more complete study and compare with the state-of-art materials in industry. Therefore, for both understanding the impact of SSA and PSD and also practical application of these materials, it is important to prepare carbon materials using the more conventional or other scalable approaches at large scale and more importantly with both different SSA and controlled PSD.

Furthermore, for the theoretical study of the impact of SSA and PSD on the capacitance performance of sp² carbon materials, due to the solvation of electrolyte ions in aqueous or organic electrolyte systems, it is not easy to study the characteristic capacitance performance of carbon materials since the specific capacitance of carbon materials in these electrolyte systems is varied with the change of d value (the thickness of electric double layer, which is the distance between the center of electrolyte ions and adjacent pore walls and is dependent on the degree of solvation of the electrolyte ions).[15] This means that the models based on solved electrolyte ions such as the popular tetraethylammonium tetrafluoroborate in acetonitrile ($TEABF_4/AN$) or propylene carbonate ($TEABF_4/PC$) systems are not the preferable systems for the study and evaluation of material's capacitance performance. To eliminate the dependence of d value, there should be no solvent molecule between the electrolyte ions and adjacent pore walls so that the d value is constant and only dependent on the size of the electrolyte ions. Thus, a more convenient system for such studies could be the solvent-free system such as using ionic liquid (IL) electrolytes, where no such complicating solvation exists.[17]

In this work, various sp² carbon materials with different (but high, and the effective) SSA and controlled PSD were prepared through a facile and low-cost method by using different carbon sources and adjusting the activation parameters such as carbon source, activation agent, amount of activation agent and activation temperature. All these materials can be prepared easily at large scale. Then, using the most recommended methods and industry practice,[5,25] the device performance of different carbon materials was evaluated and compared in two IL electrolytes with different ion size. A clear relationship between the capacitance performance and E-SSA (not SSA) was established for these carbon materials. Based on this systematic investigation, a general model for the electric double-layer capacitors is proposed for the estimation of the specific capacitance of sp² carbon materials in IL electrolytes. The good agreement between experimental and theoretical capacitance results further suggest that our model is appropriate for the evaluation of theoretical specific capacitance of various sp² carbon materials, which offers a simple yet reliable vehicle to help the design and screening of the materials for high-performance supercapacitor and other surface area related device applications.

■ EXPERIMENTAL SECTION

Materials. Phenol, formaldehyde aqueous solution (37 wt %), potassium hydroxide (KOH), sodium hydroxide (NaOH), potassium carbonate (K_2CO_3), zinc chloride ($ZnCl_2$), calcium oxide (CaO), and phosphoric acid (H_3PO_4) were commercially available from Tianjin

Guangfu Co., Ltd. All reagents were analytical grade and used as received without further purification. Graphene oxide (GO) was prepared using modified Hummers method from flake graphite.[26,27] Cork and industrial phenolic resin (iPF) were purchased from commercially available products. Poly(tetrafluoroethylene) (PTFE, Dupont), commercial AC (RP20, Kuraray Chemicals), and IL electrolytes including 1-ethyl-3-methylimidazolium tetrafluoroborate ($EMIMBF_4$, Novolyte) and 1-butyl-3-methylimidazolium tetrafluoroborate ($BMIMBF_4$, Novolyte) were all purchased and used without further purification. The cellulose film (TF4840, NKK) were used as separator for supercapacitor.

Preparation of Various sp² Carbon Materials. The preparation of various carbon materials following a modified procedure in our previous report which includes a hydrothermal carbonization process followed by an industry chemical activation step.[9] For different carbon sources, the optimization procedure is different. For the carbon source cork or iPF, 20 g of cork or iPF was added into 80 mL of water, which was stirred about for 1 h to form homogeneous suspension. When GO was used as the carbon source, 0.7 g of GO was homogeneously dispersed in 70 mL of water by ultrasonication to form a stable aqueous dispersion. When the mixture of phenol and formaldehyde aqueous solution (PF) was used as the carbon source, the weight ratio of phenol (P) to formaldehyde aqueous solution (F) employed was kept at 0.7, and 16.8 g of PF (total weight of phenol and formaldehyde aqueous solution) was homogeneously dispersed in 70 mL of water by ultrasonication to form a stable aqueous dispersion. For the carbon sources PF24GO and PF100GO (the weight ratio of P to F was kept at 0.7 and the weight ratio of PF to GO is 24 and 100, respectively), 0.3 g of GO was first homogeneously dispersed in 30 mL of water by ultrasonication to form a stable aqueous dispersion of GO. Then 7.2 and 30 g of PF were added to the GO solution respectively and stirred for 30 min to form homogeneous solution. After the dispersion step, all the as-prepared suspensions or solutions above were transferred to a 100 mL Teflon-lined autoclave. The autoclaves were sealed and heated at 180 °C for 12 h to finish the hydrothermal carbonization process. The resulted solid product was then filtered, washed three times and dried in vacuum at 120 °C for 24 h to get the hydrochars (hydrothermal products of carbon sources). For the chemical activation process, all the hydrochars was mixed with different activation agents, then heated to the target temperature at the heating rate of 5 °C/min in a horizontal furnace under Argon gas flow and held at the target temperature for 1 h. After cooling down to room temperature, the resulted products were then thoroughly washed with 10 wt % HCl to remove the residual inorganic salts, and then with distilled water until pH value reached ∼7. Finally, the resulted products were dried in an oven at 120 °C for 12h.

Characterization. Combustion elemental analysis (EA) was done at Vario Micro cube, (Elementar, Germany) for determination of the C, H and O content. Scanning Electron Microscopy (SEM) was performed on a LEO 1530 VP field emission scanning electron microscope with acceleration voltage of 10 kV. Transmission electron microscopy (TEM) was carried on Philips T20ST electron microscope at acceleration voltage of 200 kV. Electron energy loss spectroscopy (EELS, Gatan) were carried on a JEOL TEM-2100 electron microscope at acceleration voltage of 200 kV. The nitrogen adsorption/desorption analysis was done at 77 K on a Micromeritics ASAP 2020 apparatus. The Brunauer−Emmett−Teller (BET) SSA was obtained by the BET method based on the adsorption data in the relative pressure (P/P_0) range of 0.05 to 0.3. The total pore volume was measured from the amount of nitrogen adsorbed at a relative pressure (P/P_0) of 0.99. The PSD was analyzed using a nonlocal density functional theory (NL-DFT) method with a slit pore model from the nitrogen adsorption data.[8,10]

Fabrication of Supercapacitors. The industry-level two-electrode symmetrical supercapacitors based on our products and the commercial and comparing sample RP20 were fabricated to determine the capacitance performance. Briefly, 90 wt % products and 10 wt % PTFE were homogeneously mixed in the agate mortar. Note no conducting filler was used due to the high conductivity for our products as discussed below. Then the mixture was rolled into 100−

120 μm thickness sheets and punched into 18 mm diameter electrodes. After dried at 120 °C for 6 h under vacuum, the electrodes were weighted and hot pressed onto the current collectors (aluminum foils with conducting carbon coating) and then dried at 180 °C for 6 h under high vacuum to completely remove water. The dry electrodes/collectors were transferred into a glovebox filled with Ar to construct two-electrode symmetrical supercapacitors, which consist of two current collectors, two active electrodes with identical weight and a porous cellulose separator sandwiched in a test fixture consisting of two stainless steel plates. The total active material in each device is around 20 mg. EMIMBF$_4$ and BMIMBF$_4$ were used as IL electrolytes, respectively.

Evaluation of the Capacitance Performance of the sp^2 Carbon Materials. Galvanostatic charge–discharge cycle tests were measured using an Arbin testing system (Arbin MSTAT, America) at current density of 1 A/g, based on the mass of a single electrode. The gravimetric specific capacitance, C (F/g), was calculated according to

$$C = \frac{4I}{m\ \mathrm{d}V/\mathrm{d}t}$$

where I is the constant current (A), m is the total mass of the active materials on the two single electrodes (g) and $\mathrm{d}V/\mathrm{d}t$ (V/s) is the slope obtained by fitting a straight line to the discharge curve over the range from V (the voltage at the beginning of discharge) to $V/2$.

Theoretical Calculation of Diameter of Electrolyte Ions. The geometry structure of the cations and anions in all the electrolytes have been optimized by using DFT calculations (B3LYP/6-31G*),[28,29] and the frequency analysis was followed to ensure that the optimized structures were stable states. The diameter was taken from the farthest atoms distance in cations or anions. All of the DFT calculations in this paper were performed with the Gaussian 09 program package (Gaussian 09, Revision B.01, Gaussian, Inc., Wallingford CT, 2010, see Supporting Information for full citation.)

■ RESULTS AND DISCUSSION

As mentioned above, a series of sp^2 carbon materials were prepared by hydrothermal carbonization using different carbon sources and followed by chemical activation under different conditions. The applied carbon sources included cork, iPF, GO, PF, PF24GO, and PF100GO, respectively. During the hydrothermal carbonization process, carbon sources were partially reduced or *in situ* polymerized to get the hydrochars,[8,30–32] which were denoted as cork-H, iPF-H, GO-H, PF-H, PF24GO-H, and PF100GO-H, respectively. These hydrochars were further chemically activated with different activation methods, including using different activation agents, different amount of activation agent and different activation temperature. We found that the products prepared by treating the hydrochars with 4 times weight of KOH at 900 °C for 1h exhibited highest SSA (see more details in the below), which were denoted as cork-HA, iPF-HA, GO-HA, PF-HA, PF24GO-HA, and PF100GO-HA, respectively. The suffix "H" and "A" represented the products of hydrothermal process and activation process, respectively. The results of elemental analyses for the final products were listed in Table S1, which demonstrates that all the products mainly consist of carbon (more than 95 wt %), with little amount of hydrogen and oxygen. EELS characterization demonstrates that the sp^2 carbon makes up almost entirely the carbon (Figure S1).[33] For example, PF24GO-HA was found to have 96% sp^2 carbon atom, with the assumption/comparison that the sp^2 carbon atom in the graphite reference spectra is 100%. This is consistent with our and other reports.[9,10] The detailed investigation of the structure and morphology of these materials demonstrates that the addition of small amount of

GO play a key role to control the SSA and PSD and the morphology, which is discussed below.[9]

Controlling the SSA of the sp^2 Carbon Products. Thorough studies have been performed on increasing and controlling the SSA of the sp^2 carbon products. Since we have found generally the SSA and conductivity of the product from the mixture of PF and GO as the carbon source gave good results,[9] we first used it as the carbon source to study the influence of different activation agents on the SSA of final products, which included KOH, NaOH, K$_2$CO$_3$, ZnCl$_2$, H$_3$PO$_4$, and CaO.[10,34−38] As shown in Figure 1a, for the same
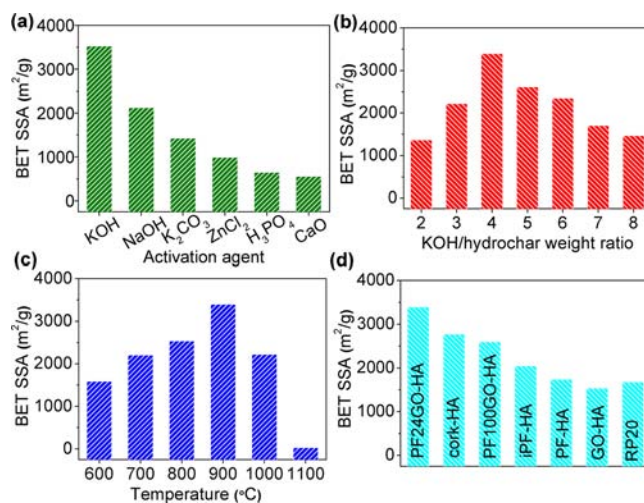

Figure 1. Controlling the SSA of sp^2 carbon materials by changing the activation parameters and carbon sources. (a) Activation agents. The BET SSA of products is controlled and varied from ~500 to ~3400 m^2/g with different activation agents. (b) Weight ratio of activation agent to hydrochar. The BET SSA was first increased from ~1300 m^2/g to ~3400 m^2/g and then gradually decreased to ~1500 m^2/g with increasing amount of activation agent. (c) Activation temperature. The BET SSA was first increased from ~1600 m^2/g to ~3400 m^2/g and then rapidly decreased to 27 m^2/g with increasing activation temperature. (d) Carbon sources. With the same activation method, all the products exhibited good BET SSA and the BET SSA is controlled and varied in the range of 1500 to 3400 m^2/g by using different carbon sources.

hydrochar of PF24GO-H, the BET SSA of the products is varied from ~500 to 3400 m^2/g with different activation agents, indicating that the SSA of the products can be controlled by using different activation agents, due to the different activity of the activation agents. Similar results were also observed for the hydrochar of iPF-H (Figure S2a).

Second, the controlling of SSA was realized by changing the weight ratio of activation agents to hydrochars. For example, for the activation agent of KOH which gave the best BET SSA results among all the activation agents, the weight ratio of KOH to the hydrochars was varied from 2 to 8 and the corresponding BET SSA was first increased from ~1300 m^2/g to ~3400 m^2/g and then gradually decreased to ~1500 m^2/g (Figure 1b). The highest SSA is achieved when the weight ratio of KOH to the hydrochars is 4. Similar results were also observed for the hydrochar of iPF-H (Figure S2b) and the common results demonstrated a great influence of the weight ratio of activation agents on the SSA, which can be applied for controlling SSA.[10,14]

Furthermore, temperature effect on the SSA of these sp^2 carbon materials was also studied by varying the temperature from 600 to 1100 °C in increments of 100 °C with KOH/hydrochar weight ratio of 4. Figure 1c shows the dependence of BET SSA on activation temperature. We can see that with increasing activation temperature from 600 to 1100 °C, the BET SSA of the activated products was first increased from ~1600 m^2/g to ~3400 m^2/g and then rapidly decreased to 27 m^2/g. The best result came from the products under activation temperature of 900 °C. This is because the activity of KOH was highly increased from 600 to 900 °C[14,39] but with further increasing temperature to the extreme high state of 1100 °C, the collapse of the porous structure and the heat-graphitization both highly decreased the SSA of carbon materials.[9,14]

Finally, the controlling of SSA was studied by using different carbon sources. From Figure 1d we can see that with the same activation method by treating these hydrochars with the optimized 4 times weight of KOH at 900 °C for 1h, all the products exhibited good to excellent BET SSA and the BET SSA is varied in the range of 1500 to 3400 m^2/g by using different carbon sources. This is probably due to the morphology difference in the hydrochars.[9] As shown in Figure 2, for the products which exhibited relatively high SSA, their
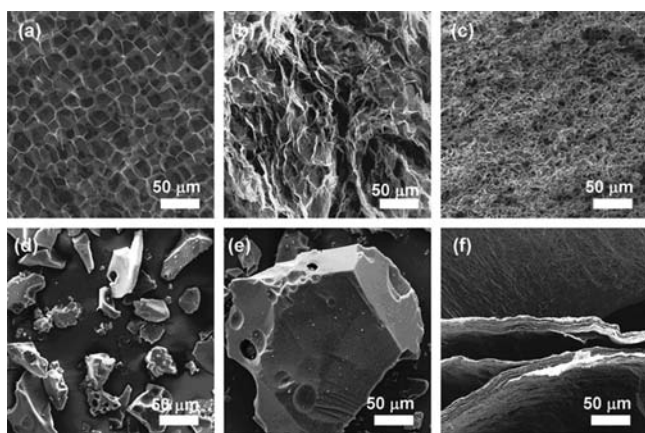
Figure 2. SEM images which show the morphology of hydrochars from different carbon sources. (a) cork-H, (b) PF24GO-H, (c) PF100GO-H, (d) iPF-H, (e) PF-H, and (f) GO-H. The morphology of these hydrochars is determined by the carbon sources and can be controlled by adding different amount of GO in the carbon source of PF. For example, compared PF-H (firm solid morphology) with PF100GO-H (loose and porous morphology), the addition of only 1 wt % GO in the carbon source of PF resulted in significant change in their morphology of hydrochars. The different morphology in these hydrochars can lead to completely different SSA and PSD in their activation products.

precursors (hydrochars) exhibited loose and porous morphology, such as cork-H and PF24GO-H, while the precursors such as iPF-H, and PF-H which showed rather firm and solid morphology gave relatively low SSA in the products. This is because the loose and porous morphology of cork-H and PF24GO-H made them much easier to mix and react with KOH to achieve higher SSA in the final products.[9] Furthermore, it is worthwhile to notice that the morphology of hydrochars can be highly modified by adding small amount of GO in the carbon sources. For example, compared PF-H (firm solid morphology) with PF100GO-H (loose and porous morphology), the addition of less than 1 wt % GO in the

carbon source of PF resulted in completely different morphology in their hydrochars. And the morphology can be further adjusted by adding different amount of GO, such as PF24GO-H and PF100GO-H. These results demonstrate that the SSA of the products is strongly related to the morphology of hydrochars, which can be controlled by using different carbon sources.
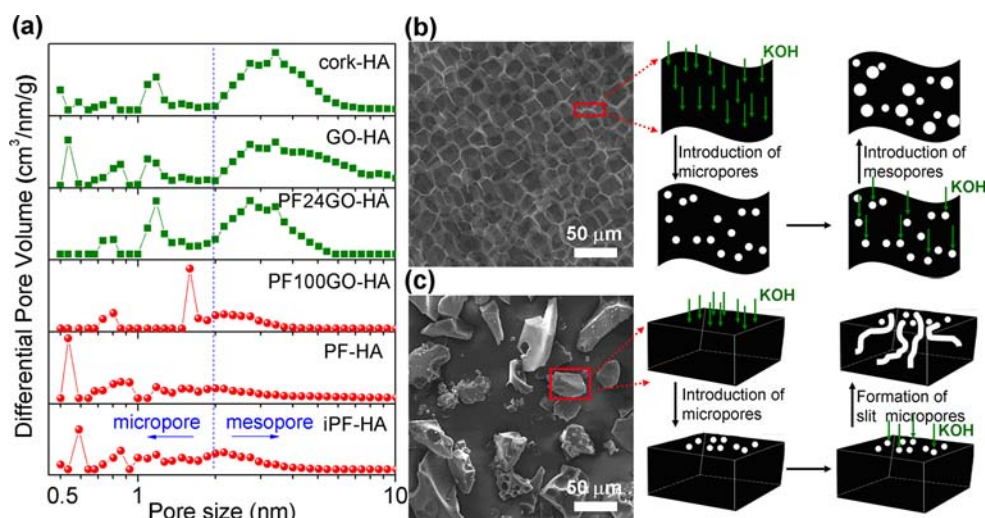
Controlling the PSD of the sp^2 Carbon Products. Previous studied have suggested that the PSD of carbon materials can also be controlled by using different carbon sources and adjusting the activation parameters.[14,38] However, we aimed at preparing a series of sp^2 carbon materials with both different (but high) SSA and controlled PSD at large scale for a systematic study From above results, the SSA of the products prepared using different activation agents other than KOH exhibited a generally lower BET SSA (Figures 1a and S2a). Thus, for a better and systematic comparison, we focused on the materials produced using the optimized KOH activation procedure from different carbon sources to study the SSA and PSD impact for these sp^2 carbon materials.

The PSD of all the products and RP20 were analyzed on the basis of the NL-DFT method with a slit/cylindrical pore model from the nitrogen adsorption data. The typical hysteresis loop found between the adsorption and desorption branches in the N$_2$ adsorption/desorption isotherms indicates the existence of abundant mesopores in the cork-HA, PF24GO-HA, and GO-HA, while the other products have no hysteresis loop and are thus mainly microporous characteristic (Figure S3).[8,40] The existence of mainly mesopores in the products of cork-HA, PF24GO-HA, and GO-HA was further identified by TEM characterization (Figure S4a−c), while there is no obvious mesopore in iPF-HA, PF-HA, and PF100GO-HA (Figure S4d−f).

Further quantitative studies for the distribution of pore volume were shown in Figure 3a, together with Table 1. Note the mesopores are defined as the pores with size over 2 nm, while the pores with smaller than that is defined as micropores.[41] From Table 1 we can see that for product iPF-HA, only ~32% pore volume was contributed by mesopores, while that was ~79% for product cork-HA. This indicates that the PSD of the products can be very different by using different carbon sources due to the different morphology of the precursors (seeing SEM images in Figure 3b,c). Similar results can be seen for PF-HA and GO-HA, in which ~25% and ~75% pore volume was contributed by mesopores, respectively. Importantly, comparing PF-HA with PF100GO-HA, we found that if we added only less than 1% of GO in PF and used the mixture precursor as the carbon source, the pore volume contributed by mesopores increased from ~25% for PF-HA to ~41% for PF100GO-HA. More dramatic change could be seen for product PF24GO-HA, where ~4% of GO addition brings the meso size pore contribution to ~67% from ~25% of that in product PF-HA. These results demonstrated that the PSD of the products can be also adjusted by changing the amount of GO in the carbon sources.

The reason why different carbon sources under same conditions resulted in completely different PSD in their sp^2 carbon products could be ascribed to the structural difference in their hydrochars. From the SEM images in Figure 2 we can see that for the products which have more mesopores, their precursors such as cork-H, PF24GO-H and GO-H exhibited some layered and/or porous (no matter the sheets were randomly or orderly stacked, Figure 2a−c). But for those which

Figure 3. Controlling the PSD of sp² carbon materials. (a) PSD of all the products based on the NL-DFT method with a slit/cylindrical pore model from the nitrogen adsorption data. The PSD of the products is controlled and varied from micropores to mesopores with different carbon sources under same conditions. (b) A typical SEM image of cork-H, showing the unique porous/layered structure and the likely mechanism for the formation of mesopores. (c) A typical SEM image of iPF-H, showing a more firm and solid and the mechanism for the formation of slit/cylindrical micropores.

Table 1. Distribution of Pore Volume for All the Products and RP20

product	pore volume ($cm^3\ g^{-1}$)	micropore[a] (%)	mesopore[b] (%)
cork-HA	1.98	21	79
GO-HA	1.12	25	75
PF24GO-HA	1.78	33	67
PF100GO-HA	1.04	59	41
PF-HA	0.77	75	25
iPF-HA	0.88	68	32
RP20	0.64	94	6

[a]Percent of pore volume contributed by micropores. [b]Percent of pore volume contributed by mesopores. The mesopores are defined as the pores with size over 2 nm, while the pores with smaller than that is defined as micropores.

have more micropores, the precursors such as iPF-H and PF-H showed a more firm and solid structure (Figure 2d,e). According to the fractal structure theory,[42,43] the origin of micropores and mesopores was basically identical regardless of their pore sizes: the mesopores were formed by further activation process of micropores, including pore widening, fusing and wall collapsing.[44] Thus, we believe that the unique porous/layered structure in cork-H, GO-H, and PF24GO-H make them much easier to undergo the further activation process of micropores, which can produce abundant mesopores. So it is critical important to control the precursor morphology to achieve the required PSD. The likely mechanism for the formation of mesopores is proposed as shown in Figure 3b. In another situation, due to the large particles with firm solid structure in iPF-HA and PF-HA, chemical activation occurs probably via the "drilling" of potassium-containing clusters to form predominantly slit/cylindrical micropores (Figure 3c).[42−44]

Influence of SSA, PSD, and E-SSA on Supercapacitor Performance. In order to study the influence of SSA, PSD and E-SSA on the supercapacitor performance, we have evaluated the capacitance performance of all the sp² carbon products and the control sample RP20 using the best-recommended industry

practice and method for the fabrication and characterization of practical supercapacitor devices.[5,25,45] Two IL electrolytes with different size of positive ions were used for a more systematic study. Galvanostatic charge−discharge curves of all the products in IL electrolytes of $EMIMBF_4$ and $BMIMBF_4$ were shown in the Figures 4a and S5, respectively. All the discharge curves are linear in the total range of potential, showing nearly perfect capacitive behavior.[4] The specific capacitance was obtained from the discharge curves at the current density of 1 A/g. The detailed specific capacitance was summarized in Table 2.

The DFT SSA and the distribution of DFT SSA with pore size were measured on the basis of the slit/cylindrical NL-DFT model[10,46] from the experimental nitrogen adsorption data and shown in Figure 4b. The inset vertical dashed line demonstrated the diameter of positive ions for two IL electrolytes. As solvent-free electrolytes, ILs offer the unique advantage of a well identified ion size since no solvation shell can form.[17] Note the diameter of positive ions are 0.75 and 1.11 nm for $EMIM^+$ and $BMIM^+$, respectively, which are both much larger than the diameter of negative ions. So the size of the positive ions are used for the evaluation and modeling following. The E-SSA of electrode materials in different electrolytes was defined as the cumulative DFT SSA of pores with size above the diameter of positive ions in IL electrolytes.

The detailed DFT SSA and E-SSA of all the materials, together with the capacitance, in two IL electrolytes were listed and compared in Table 2. From these data, several conclusions can be drawn. First, it is important to note that PSD is equally important if not more important to determine E-SSA and both high total SSA and a matchable PSD are needed to achieve high E-SSA. For example, cork-HA and PF24GO-HA exhibit close total DFT SSA (1767 and 1779 m^2/g, respectively), but their different PSD leads to very different E-SSA (1378 and 1657 m^2/g, respectively). The impact of total SSA but with similar PSD could be seen from products of PF24GO-HA and GO-HA, which exhibit similar mesoporous property (67% and 75% pore volume was contributed by mesopores, respectively), but the total DFT SSA of PF24GO-HA (1779 m^2/g) is much

5925

dx.doi.org/10.1021/ja402552h | J. Am. Chem. Soc. 2013, 135, 5921−5929
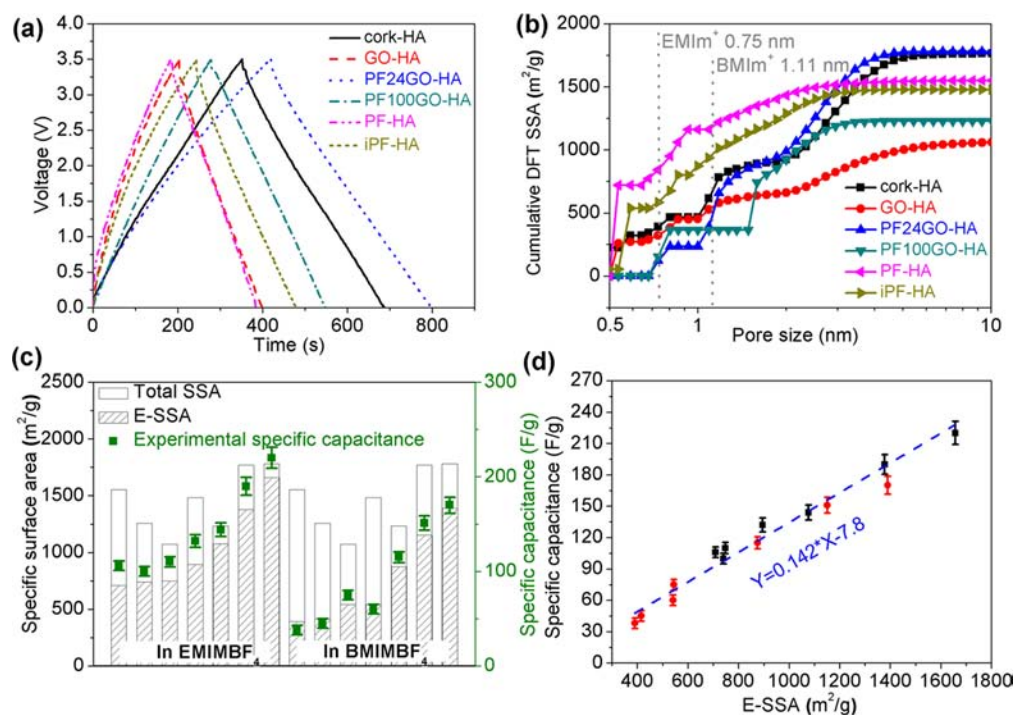
Figure 4. (a) Galvanostatic charge−discharge curves of supercapacitors based on all the products in EMIMBF$_4$ electrolyte, at current density of 1 A/g. (b) The distribution of DFT SSA with pore width for all the products. The inset vertical dashed line demonstrated the diameter of positive ion for two IL electrolytes. (c) Relationship between the specific capacitance and E-SSA. The E-SSA was defined as the cumulative DFT SSA of pores with size above the ion diameter of different electrolytes. The specific capacitance was positively related to the E-SSA (but not the total SSA) of the products in the electrolytes. The statistical deviation of experimental specific capacitance is about ±5%. (d) Linear relationship for the plotting of specific capacitance vs E-SSA. The black and red points represent the specific capacitance and E-SSA data of the sp^2 products in EMIMBF$_4$ and BMIMBF$_4$, respectively. The slope of the fitting line is 0.142, with the coefficient of determination of 0.96, indicating a good linear relationship between the specific capacitance and E-SSA.

Table 2. E-SSA^a and Corresponding Experimental Specific Capacitance of All the Products and RP20 in IL Electrolytes of EMIMBF$_4$ and BMIMBF$_4$, Respectively

| product	DFT SSA (m^2/g)	E-SSA for EMIMBF$_4$^{b} (m^2/g)	capacitance in EMIMBF$_4$ (F/g)	E-SSA for BMIMBF$_4$^{c} (m^2/g)	capacitance in BMIMBF$_4$ (F/g)
PF24GO-HA	1779	1657	220	1390	170
cork-HA	1767	1378	190	1151	151
PF100GO-HA	1230	1077	144	875	115
iPF-HA	1480	895	132	541	60
GO-HA	1071	748	110	544	75
PF-HA	1552	709	106	390	38
RP20	1255	740	100	415	45

^{a}The E-SSA of electrode materials in different electrolytes was defined as the cumulative DFT SSA of pores with size above the diameter of positive ions in IL electrolytes. The specific capacitance was obtained from the discharge curves at the current density of 1 A/g. All the experimental values presented are the averaged values and the statistical deviation is about ±5%. ^{b}The diameter of EMIM$^+$ is 0.75 nm. ^{c}The diameter of EMIM$^+$ is 1.11 nm.

higher than that of GO-HA (1071 m^2/g), which resulted in a much higher E-SSA of PF24GO-HA (1657 m^2/g) in EMIMBF$_4$ than that of GO-HA (748 m^2/g).

More important conclusion can be seen from Figure 4c, which shows the relationship between total SSA and E-SSA with the specific capacitance for all the different products. We can see that for both two IL electrolytes, the specific capacitance was positively related to the E-SSA (but not the SSA) of the products in the electrolytes. A clearer relationship is demonstrated in Figure 4d for the plotting of specific capacitance vs E-SSA. The slope of the fitting line is 0.142, with the coefficient of determination of 0.96, indicating a good linear relationship between the specific capacitance and E-SSA. This

clear linear relationship indicates that the capacitance can be estimated directly and reliably using the effective surface area without fabrication of devices, speeding up the material design and screening.

There results demonstrate that it is the E-SSA which determines fundamental capacitance performance and both total SSA and PSD play important roles on the E-SSA and capacitance performance. Thus, in both IL systems, the product PF24GO-HA, with the highest E-SSA, gave the best capacitance performance.[10,12,20] Therefore, it is much more important to control the E-SSA and PSD of carbon materials in the electrolytes for better capacitance performance than just simply increase the total SSA of carbon materials.

5926

dx.doi.org/10.1021/ja402552h | J. Am. Chem. Soc. 2013, 135, 5921−5929
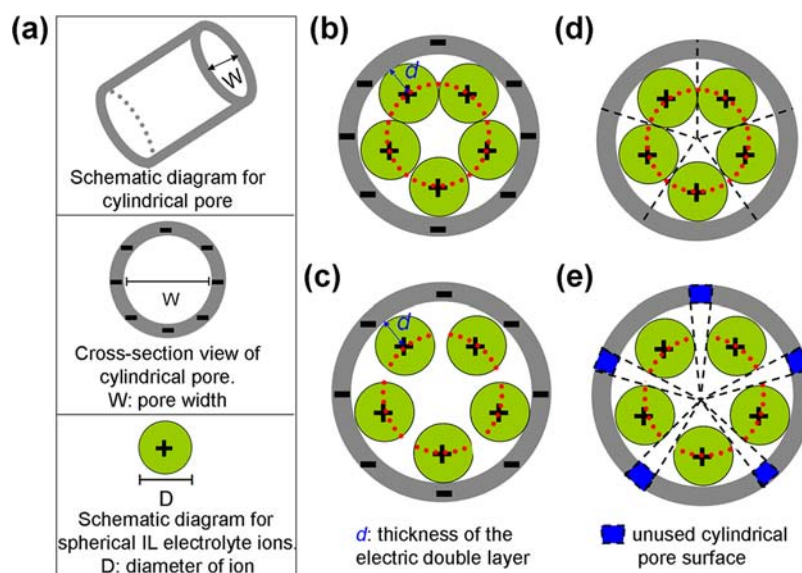
Figure 5. (a) Schematic diagrams of cylindrical pore, cross-section of cylindrical pore and spherical IL electrolyte ions. The gray cycle represents the cylindrical pore wall with negative charges and the green ball represents the positive ion of IL electrolytes. Schematic diagrams of IL electrolyte ion packing mode in pores at the state of (b) tightly stacked ions together because of the completely matching between the ion and pore size and (c) not tightly stacked together due to mismatch. The d value is equal to the radius of electrolyte ions for both the two states. Schematic diagrams (d) and (e) for the utilized cylindrical pore surface in the states of (b) and (c). The blue part in (e) represents the unused or wasted cylindrical pore surface.

Theoretical Calculation of Specific Capacitance. The theoretical specific capacitance of carbon materials in the electrolytes can be calculated according to the eq 1,

$$C = \varepsilon \varepsilon_0 A / d \qquad (1)$$

A is the E-SSA and d is the thickness of electric double layer (referred as the distance between the center of electrolyte ions and adjacent pore walls). ε_0 is vacuum permittivity which is 8.85×10^{-12} F/m, and ε is the relative dielectric constant of the electrolyte, respectively.[2,15] The value of ε is influenced by the temperature and other factors.[47] In our case, the room temperature ε was used as the measurement was carried at room temperature,[48] which are reported to be 14.8 and 12.9 for EMIMBF$_4$ and BMIMBF$_4$ electrolytes, respectively. Thus, we can see that C is primarily determined by A and d.[15] Note the A should be the effective surface area as defined as E-SSA, not the total surface area as discussed in many literatures, and d depends on the electrolyte ion diameter when no solvent exists as in the case of IL systems. In order to get the A and d values, we built a model based on the spherical IL electrolyte ions and carbon materials with cylindrical pore surface (Figure 5a).

Previous studies from Dzubiella and Hansen showed that under a potential, there is substantial ion motion in pores.[49] So we assume that there are as many ions in those cylindrical pores as possible allowed by space and an electric double layer is formed between the center of electrolyte ions and the adjacent pore walls due to the electrostatic absorption. And for solvent-free IL ions, there is no solvation shell around the IL ions due to the absence of solvent molecules, while for aqueous and organic electrolytes, the solvent molecules will be filled between electrolyte ions and adjacent pore walls when the electrolyte ions in the pores are not tightly stacked, which resulted in variable d value and also complicated the modeling.[15] Therefore, on the basis of all these above, we assume that for IL electrolyte systems, the value of d is always equal to the radius of electrolyte ions no matter the electrolyte ions in the pores are tightly stacked or not (Figure 5b,c).

Moreover, for IL electrolyte systems, the utilized surface area is strongly influenced by the matching between the pore size and the size of IL ions. As an example shown in Figure 5d, when the relationship between pore width and ion size satisfies the tight packing mode of the electrolyte ions in the pores (certain amount of ions can occupy completely the entire surface area), the cylindrical pore surface is fully occupied and the utilized surface area can reach 100%. But when the electrolyte ions cannot tightly pack together inside the pores due to mismatch of pore width and ion size, there are some unused or wasted cylindrical pore surface (the blue parts shown in Figure 5e), the utilized E-SSA (UE-SSA) will be less than 100%. The proportion of UE-SSA in the entire E-SSA is dependent on the relationship between the pore width and size of electrolyte ion and can be calculated according to the mathematical and geometric methods (Figure S6). Detailed mathematical formulas and calculation methods are shown in the Supporting Information.

Therefore, based on slit/cylindrical NL-DFT model from the experimental nitrogen adsorption data of the products and the ion size of the electrolytes, we can get the E-SSA and distribution of E-SSA with pore size in the products. That means for a given pore size, we can get the corresponding E-SSA contributed by the pores at this size. Then we can get the UE-SSA according to the relationship between the given pore size and ion size of electrolytes and calculate out the specific capacitance contributed by the pores at this size. Finally, the cumulative specific capacitance of the products with a certain PSD and E-SSA can be obtained by summarizing the specific capacitance contributed by all the pores in the products. As one typical example for the theoretical calculation of specific capacitance, the detailed E-SSA, UE-SSA and specific capacitance of the pores in PF24GO-HA for EMIMBF$_4$ and BMIMBF$_4$ electrolytes are shown in Tables S2 and S3, respectively. The cumulative specific capacitance of PF24GO-HA in EMIMBF$_4$ and BMIMBF$_4$ electrolytes is 445 F/g and 240 F/g, respectively. And the cumulative specific capacitance
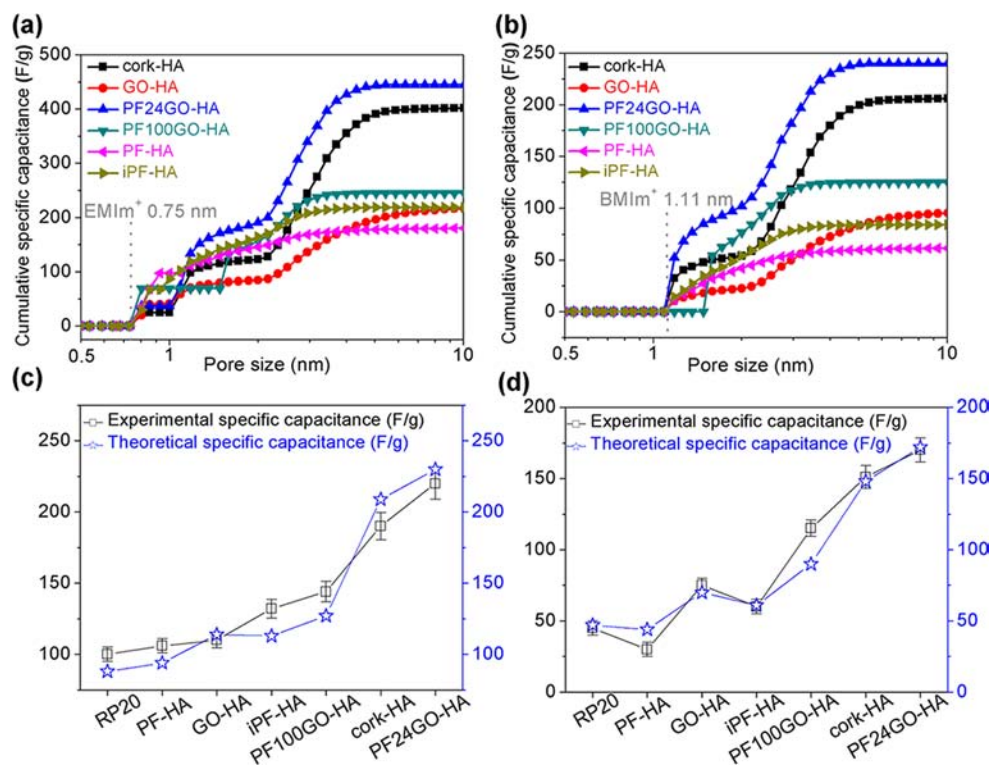
Figure 6. Cumulative specific capacitance of all the sp^2 carbon products in IL electrolytes of (a) EMIMBF$_4$ and (b) BMIMBF$_4$. The cumulative specific capacitance of all the products in each kind of IL electrolyte was normalized by the same degree to get the normalized cumulative specific capacitance, which is defined as theoretical specific capacitance of the products in the IL electrolytes. Relationship between the experimental and theoretical specific capacitance of various carbon materials in IL electrolytes of (c) EMIMBF$_4$ and (d) BMIMBF$_4$. The statistical deviation of experimental specific capacitance is about ±5%. Excellent agreement between experimental and theoretical specific capacitance was obtained for various carbon materials with different effective surface areas in both two IL electrolytes, indicating that the model for the calculation of theoretical specific capacitance is appropriate for supercapacitors based on various sp^2 carbon materials in IL electrolytes.

of all the other products and RP20 in EMIMBF$_4$ and BMIMBF$_4$ were calculated by the same method and shown in Figures 6a,b and S7.

Note the values of cumulative specific capacitance are quite away from the experimental specific capacitance. For example, for PF24GO-HA-based supercapacitors in EMIMBF$_4$ electrolyte, the experimental and cumulative specific capacitance are 220 F/g and 445 F/g, respectively. The exact reasons behind this inconsistency are not fully understood, but one possible reason could be the actual relative dielectric constant of the IL electrolyte (ε'), which could vary due to many reasons such as the curvature of the pore surface, the temperature and frequency dependency of relative dielectric constant.[47] Therefore, the cumulative specific capacitance of all the products in each kind of IL electrolyte was normalized by the same degree to get the normalized cumulative specific capacitance. As one example for the EMIMBF$_4$ electrolyte system, the cumulative specific capacitance of all the products is divided by 2.0, since the cumulative specific capacitance of PF24GO-HA-based supercapacitors (445 F/g) in EMIMBF$_4$ electrolyte is 2.0 times as large as the experimental specific capacitance (220 F/g). Similarly, the cumulative specific capacitance of all the products is divided by 1.4 for the other BMIMBF$_4$ electrolyte system. (For PF24GO-HA-based supercapacitors in BMIMBF$_4$ electrolyte, the experimental and cumulative specific capacitance was 170 F/g and 238 F/g, respectively.)

The normalized cumulative specific capacitance is then defined as theoretical specific capacitance and compared with experimental specific capacitance, as shown in Figure 6c,d.

From these figures an excellent agreement between experimental and theoretical specific capacitance for all the products and RP20 in both two IL electrolytes is observed, indicating that our model for the calculation of theoretical specific capacitance is appropriate for supercapacitors based on various carbon materials in IL electrolytes. Thus, with the experimental SSA and PSD measured easily from such as nitrogen adsorption/desorption analysis for any material, its supercapacitor performance can be estimated quite reliably without fabricating the actual device using our model and the equation $C(F/g) = 0.142 \times$ E-SSA $(m^2/g) - 7.8$ as shown in Figure 4d, which indicates that materials with high E-SSA could achieve high-capacitance performance. This obviously would greatly improve the designing and screening of new material development.

CONCLUSION

Controlling the SSA and PSD of sp^2 carbon materials has been realized by using different carbon sources or adjusting the preparation parameters. Both the experimental results and theoretical calculation of specific capacitance indicate that the capacitance performance of carbon materials in IL systems is strongly dependent on the E-SSA with an excellent linear relationship, which is determined by both conventional SSA and PSD. A model is proposed to predict the theoretical capacitance for these sp^2 carbon materials using the equation $C(F/g) = 0.142 \times$ E-SSA $(m^2/g) - 7.8$, which is in excellent agreement with the experimental results. Thus, our model could be used to guide and speed up the design of new sp^2

5928

dx.doi.org/10.1021/ja402552h | J. Am. Chem. Soc. 2013, 135, 5921−5929

carbon materials for better supercapacitor performance and other surface area related device applications.

■ ASSOCIATED CONTENT

Ⓢ Supporting Information

Characterization of various carbon materials by TEM and EELS, and other supplementary figures. This material is available free of charge via the Internet at http://pubs.acs.org.

■ AUTHOR INFORMATION

Corresponding Author

yschen99@nankai.edu.cn

Notes

The authors declare no competing financial interest.

■ ACKNOWLEDGMENTS

■ REFERENCES

(1) Simon, P.; Gogotsi, Y. Nat. Mater. 2008, 7, 845.

(2) Simon, P.; Gogotsi, Y. Acc. Chem. Res. 2012, DOI: 10.1021/ar200306b.

(3) Frackowiak, E. Phys. Chem. Chem. Phys. 2007, 9, 1774.

(4) Wang, Y.; Shi, Z.; Huang, Y.; Ma, Y.; Wang, C.; Chen, M.; Chen, Y. J. Phys. Chem. C 2009, 113, 13103.

(5) Gogotsi, Y.; Simon, P. Science 2011, 334, 917.

(6) Wan, X.; Huang, Y.; Chen, Y. Acc. Chem. Res. 2012, 45, 598.

(7) Hall, P. J.; Mirzaeian, M.; Fletcher, S. I.; Sillars, F. B.; Rennie, A. J. R.; Shitta-Bey, G.; Wilson, G.; Cruden, A.; Carter, R. Energy Environ. Sci. 2010, 3, 1238.

(8) Wei, L.; Sevilla, M.; Fuertes, A. B.; Mokaya, R.; Yushin, G. Adv. Energy Mater. 2011, 1, 356.

(9) Zhang, L.; Zhang, F.; Yang, X.; Long, G.; Wu, Y.; Zhang, T.; Leng, K.; Huang, Y.; Ma, Y.; Yu, A.; Chen, Y. Sci. Rep. 2013, 3, 1408.

(10) Zhu, Y.; Murali, S.; Stoller, M. D.; Ganesh, K.; Cai, W.; Ferreira, P. J.; Pirkle, A.; Wallace, R. M.; Cychosz, K. A.; Thommes, M.; Su, D.; Stach, E. A.; Ruoff, R. S. Science 2011, 332, 1537.

(11) Ghosh, A.; Lee, Y. H. Chemsuschem 2012, 5, 480.

(12) Jha, N.; Ramesh, P.; Bekyarova, E.; Itkis, M. E.; Haddon, R. C. Adv. Energy Mater. 2012, 2, 438.

(13) Li, Q. Y.; Wang, H. Q.; Dai, Q. F.; Yang, J. H.; Zhong, Y. L. Solid State Ionics 2008, 179, 269.

(14) Murali, S.; Potts, J. R.; Stoller, S.; Park, J.; Stoller, M. D.; Zhang, L. L.; Zhu, Y.; Ruoff, R. S. Carbon 2012, 50, 3482.

(15) Chmiola, J.; Yushin, G.; Gogotsi, Y.; Portet, C.; Simon, P.; Taberna, P. Science 2006, 313, 1760.

(16) Inagaki, S.; Oikawa, K.; Kubota, Y. Chem. Lett. 2009, 38, 918.

(17) Largeot, C.; Portet, C.; Chmiola, J.; Taberna, P. L.; Gogotsi, Y.; Simon, P. J. Am. Chem. Soc. 2008, 130, 2730.

(18) Lozano-Castello, D.; Lillo-Rodenas, M. A.; Cazorla-Amoros, D.; Linares-Solano, A. Carbon 2001, 39, 741.

(19) Hayashi, J.; Horikawa, T.; Takeda, I.; Muroyama, K.; Nasir Ani, F. Carbon 2002, 40, 2381.

(20) Wei, L.; Sevilla, M.; Fuertes, A. B.; Mokaya, R.; Yushin, G. Adv. Funct. Mater. 2012, 22, 827.

(21) Gamby, J.; Taberna, P. L.; Simon, P.; Fauvarque, J. F.; Chesneau, M. J. Power Sources 2001, 101, 109.

(22) Kyotani, T. Carbon 2000, 38, 269.

(23) Choi, B. G.; Yang, M.; Hong, W. H.; Choi, J. W.; Huh, Y. S. ACS Nano 2012, 6, 4020.

(24) Sheng, Z. M.; Wang, J. N.; Ye, J. C. Micropor. Mesopor. Mater. 2008, 111, 307.

(25) Stoller, M. D.; Ruoff, R. S. Energy Environ. Sci. 2010, 3, 1294.

(26) Becerril, H. A.; Mao, J.; Liu, Z.; Stoltenberg, R. M.; Bao, Z.; Chen, Y. Acs Nano 2008, 2, 463.

(27) Zhang, L.; Liang, J.; Huang, Y.; Ma, Y.; Wang, Y.; Chen, Y. Carbon 2009, 47, 3365.

(28) Lee, C.; Yang, W.; Parr, R. G. Phys. Rev. B 1988, 37, 785−789.

(29) Becke, A. D. J. Chem. Phys. 1993, 98, 5648.

(30) Titirici, M. M.; Antonietti, M.; Baccile, N. Green Chem. 2008, 10, 1204.

(31) Berl, E.; Schmidt, A.; Koch, H. Angew. Chem. 1932, 45, 517.

(32) Hu, B.; Wang, K.; Wu, L.; Yu, S. H.; Antonietti, M.; Titirici, M. M. Adv. Mater. 2010, 22, 813.

(33) Berger, S. D.; McKenzie, D. R.; Martin, P. J. Philos. Mag. Lett. 1988, 57, 285.

(34) Lillo-Rodenas, M. A.; Cazorla-Amoros, D.; Linares-Solano, A. Carbon 2003, 41, 267.

(35) Olivares-Marin, M.; Fernandez-Gonzalez, C.; Macias-Garcia, A.; Gomez-Serrano, V. J. Anal. Appl. Pyrol. 2012, 94, 131.

(36) Teng, H.; Yeh, T. S.; Hsu, L. Y. Carbon 1998, 36, 1387.

(37) Khalili, N. R.; Campbell, M.; Sandi, G.; Golas, J. Carbon 2000, 38, 1905.

(38) Lozano-Castello, D.; Cazorla-Amoros, D.; Linares-Solano, A.; Quinn, D. F. Carbon 2002, 40, 989.

(39) Molina-Sabio, M.; Rodriguez-Reinoso, F. Colloids Surf., A 2004, 241, 15.

(40) Sing, K. S. W.; Everett, D. H.; Moscou, L.; Pierrotti, R.; Roquerol, J.; Siemieniewska, T. Pure Appl. Chem. 1985, 57, 603.

(41) Corma, A. Chem. Rev. 1997, 97, 2373.

(42) Pfeifer, P.; Avnir, D. J. Chem. Phys. 1983, 79, 3558.

(43) Farin, D.; Avnir, D.; Pfeifer, P. J. Chem. Phys. 1983, 79, 3566.

(44) Shiratori, N.; Lee, K.; Miyawaki, J.; Hong, S. H.; Mochida, I.; An, B.; Yokogawa, K.; Jang, J.; Yoon, S. H. Langmuir 2009, 25, 7631.

(45) Yang, X.; Zhang, F.; Zhang, L.; Zhang, T.; Huang, Y.; Chen, Y. Adv. Funct. Mater. 2013, DOI: 10.1002/adfm.201203556.

(46) Barbieri, O.; Hahn, M.; Herzog, A.; Kotz, R. Carbon 2005, 43, 1303.

(47) Mizoshiri, M.; Nagao, T.; Mizoguchi, Y.; Yao, M. J. Chem. Phys. 2010, 132, 164510.

(48) Singh, T.; Kumar, A. J. Phys. Chem. B 2008, 112, 12968.

(49) Dzubiella, J.; Hansen, J. P. J. Chem. Phys. 2005, 122, 234706.

5929

dx.doi.org/10.1021/ja402552h | J. Am. Chem. Soc. 2013, 135, 5921−5929